SCIENTIFIC REP⚙RTS

OPEN

Field-driven dynamics and time-resolved measurement of Dzyaloshinskii-Moriya torque in canted antiferromagnet YFeO₃

Tae Heon Kim[1,2], Peter Grüenberg[2], S. H. Han[3] & B. K. Cho[1,2]

Electrical spin switching in an antiferromagnet is one of the key issues for both academic interest and industrial demand in new-type spin devices because an antiferromagnetic system has a negligible stray field due to an alternating sign between sub-lattices, in contrast to a ferromagnetic system. Naturally, questions arise regarding how fast and, simultaneously, how robustly the magnetization can be switched by external stimuli, e.g., magnetic field and spin current. First, the exploitation of ultrafast precessional motion of magnetization in antiferromagnetic oxide has been studied intensively. Regarding robustness, the so-called inertia-driven switching scenario has been generally accepted as the switching mechanism in antiferromagnet system. However, in order to understand the switching dynamics in a canted antiferromagnet, excited by magnetic field, accurate equation of motion and corresponding interpretation are necessary. Here, we re-investigate the inertia-driven switching process, triggered by the strict phase matching between effective driving field, d*h*/d*t*, and antiferromagnetic order parameters, *l*. Such theoretical approaches make it possible to observe the static parameters of an antiferromagnet, hosting Dzyaloshinskii–Moriya (DM) interaction. Indeed, we estimate successfully static parameters, such as DM, exchange, and anisotropy energies, from dynamical behaviour in YFeO₃, studied using terahertz time-domain spectroscopy.

Because the precessional motion of magnetization has been generally employed for fast magnetization switching[1–5], much attention has been paid to antiferromagnetic oxide system because of its ultrafast spin response ($\omega_{\mathrm{AF}} \sim \sqrt{JK} \sim 10^{12}\,\mathrm{s}^{-1}$), coupled with large exchange energy, J, and anisotropy energy, K[6]; such characteristics highlight its potential applicability[7–20]. The exchange interaction is found not to contribute to the precession in ferromagnetic system ($\omega_{\mathrm{F}} \sim \sqrt{K} \sim 10^{9}\,\mathrm{s}^{-1}$)[14, 21].

Moreover, inertia-driven switching in an antiferromagnet is suggested as a new switching scenario[10, 13, 22]; even after external magnetic field has been turned off, accumulated exchange energy by small disturbances works as a driving force to switch magnetization. More quantitatively, S. Wienholdt *et al.* have constructed the energetic consideration for switching; switching occurs always when the exchange gain (or kinetic energy) stored by the magnetic field is over the anisotropic (or potential) barrier[13].

Supporting inertia-like behaviour, there are several reports for the spin-current-driven switching in simple antiferromagnet[16] and canted antiferromagnet[19] with broken inversion symmetry[23]. Their works highlight the potential for practical applications by replacing the magnetic field with spin current.

However, we reconsider field-driven dynamics in canted antiferromagnet; magnetic resonances are known to exist in two branches[24] and to be selectively excited by the polarization of external stimulus: magnetic field or spin current. As a result, we found that inertia-driven switching is not induced by a magnetic field *h*(t) when magnetic field is applied, so that a reliable equation of motion for canted antiferromagnets is necessary to be set up.

Here, we investigated the field-driven dynamics in canted antiferromagnets in two regimes: a field-interaction regime and free-induction decay regime. It is found that the magnetization switching is achieved under the strict

[1]School of Materials Science and Engineering, Gwangju Institute of Science and Technology (GIST), Gwangju, 500-712, Republic of Korea. [2]Gruenberg Center for Magnetic Nanomaterials, Gwangju Institute of Science and Technology (GIST), Gwangju, 500-712, Republic of Korea. [3]Division of Navigation Science, Mokpo National Maritime University, Mokpo, 58628, Republic of Korea. Correspondence and requests for materials should be addressed to B.K.C. (email: chobk@gist.ac.kr)
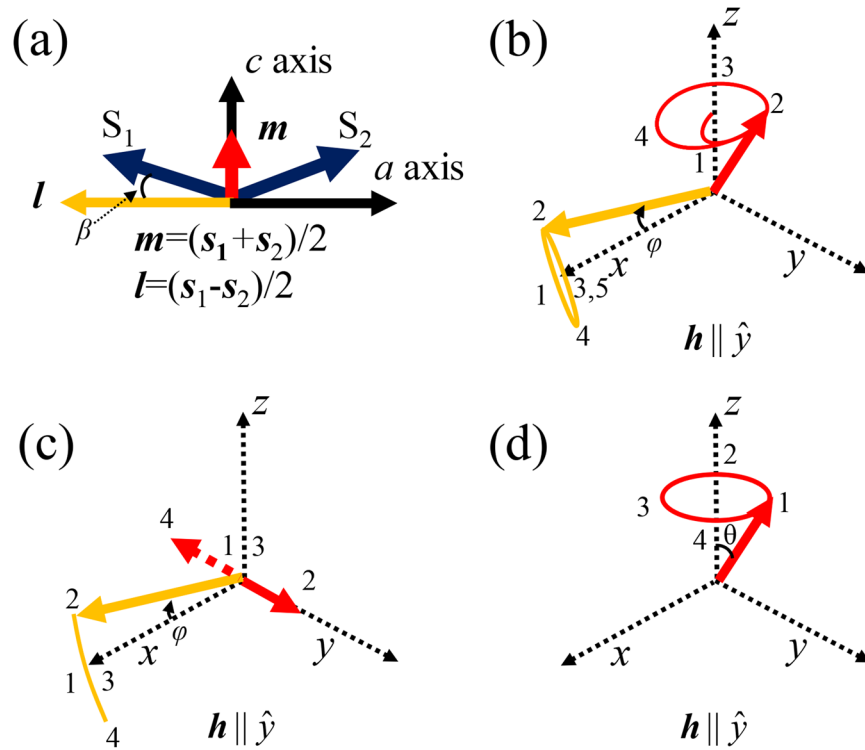
Figure 1. Spin configuration of a canted antiferromagnet in equilibrium and schematic for the excitation modes in various magnetic systems. (**a**) Equilibrium state of a canted antiferromagnet. (**b–d**) Excitation modes when the incident magnetic pulse is applied in the y-direction: (**b**) Elliptical precession in a canted antiferromagnet. (**c**) Fluctuating motion in a simple antiferromagnet and (**d**) ferromagnet precession.

phase matching between antiferromagnetic order parameters, $l=(s_1-s_2)/2$ and driving field, i.e., ~$dh(t)/dt$, consistent to the fact that antiferromagnet dynamics are fundamentally inertia-driven. The ferromagnetic order parameter, $m=(s_1+s_2)/2$ is only a slave vector. In free-induction decay regime, we demonstrate in both experiment and theory that the precessional ellipticity in Sigma mode (S-mode), one of two resonant modes[24], provides Dzyaloshinskii-Moriya (DM) energy information. The energy information is important because probing DM energy has massive potential for applications, based on the chiral spin domain[25–27] and antiferromagnetic bubble dynamics[28, 29] beyond the sub-lattice structure of an antiferromagnet.

Theory
Field-driven spin dynamics of YFeO₃. In this article, we study single crystal $YFeO_3$, a prototype for canted antiferromagnet. The magnetism of $YFeO_3$ is governed by the Fe^{3+} spins. Assuming that the spatial gradient of magnetization is absent, the magnetic properties could be described as the total energy, U, consisting of two sub-lattices, $i=1$ and 2:

$$U = Js_i \cdot s_{3-i} + D \cdot (s_i \times s_{3-i}) + K_x[(s_{i,x})^2 + (s_{3-i,x})^2]$$
$$+ K_z[(s_{i,z})^2 + (s_{3-i,z})^2] + gu_B(s_i + s_{3-i}) \cdot h. \tag{1}$$

The sub-lattices are normalized by their magnitude, e.g., $s_i = S_i/|S_i|$. The first term denotes exchange energy, where the nearest-neighbour exchange constant, J, has 63.7 meV. The second term describes DM energy, where the DM vector, D, is $-D_y\hat{y}$ with $D_y = 1.4$ meV. The third and fourth terms are two anisotropy energies where K_x and K_z are set to be 22 μeV and 9.9 μeV respectively. These energy combinations give rise to weak ferromagnetism where the anti-parallel spins are tilted slightly towards the z-axis in Fig. 1(a). The final term is Zeeman energy, where g is Landè g-factor, and u_B is Bohr magneton, which is equal to the multiplication of gyromagnetic ratio, γ, and reduced Plank constant, $\hbar$. The dynamics for our magnetic system can be described by coupled Landau-Lifshitz-Gilbert (LLG) equation:

$$\dot{s}_i = [Js_i \times s_{3-i} + (-1)^{i+1}s_i \cdot (D \times s_{3-i}) + K_x\hat{x} \times s_i + K_z\hat{z} \times s_i]/\hbar + \gamma(s_i + s_{3-i}) \times h + \alpha(s_i \times \dot{s}_i), \tag{2}$$

where the final term is magnetic damping characterized by damping coefficient, α.

Next, with $l=(s_1-s_2)/2$ and $m=(s_1+s_2)/2$, equation (2) can be written as:

$$\dot{\boldsymbol{m}} = [-\boldsymbol{D} \times (\boldsymbol{m} \times \boldsymbol{l}) + K_x\hat{x} \times (m_x\boldsymbol{m} + l_x\boldsymbol{l}) + K_z\hat{z} \times (m_z\boldsymbol{m} + l_z\boldsymbol{l})]/\hbar$$
$$+ \gamma(\boldsymbol{m} \times \boldsymbol{h}) + \alpha(\boldsymbol{l} \times \dot{\boldsymbol{l}} + \boldsymbol{m} \times \dot{\boldsymbol{m}}), \tag{3}$$

$$\dot{\boldsymbol{l}} = [2J(\boldsymbol{l} \times \boldsymbol{m}) + \boldsymbol{l} \times (\boldsymbol{l} \times \boldsymbol{D}) - \boldsymbol{m} \times (\boldsymbol{m} \times \boldsymbol{D}) + K_x\hat{x} \times (m_x\boldsymbol{l} + l_x\boldsymbol{m})$$
$$+ K_z\hat{z} \times (m_z\boldsymbol{l} + l_z\boldsymbol{m})]/\hbar + \gamma(\boldsymbol{l} \times \boldsymbol{h}) + \alpha(\boldsymbol{m} \times \dot{\boldsymbol{l}} + \boldsymbol{l} \times \dot{\boldsymbol{m}}). \tag{4}$$

In canted antiferromagnets, two resonant modes, named as S-mode and Gamma-mode (G-mode)[24], are excited selectively depending on external magnetic field polarization parallel or perpendicular to the z-axis. Here, we consider the S-mode when magnetic field is applied along the y-axis. With the effective variables, $\{l_x, m_y, l_z\}$, the following approximations can be exploited: $\boldsymbol{m} \cdot \boldsymbol{l} = 0$, $|\boldsymbol{m}|^2 + |\boldsymbol{l}|^2 = 1$, $|\boldsymbol{m}| \ll |\boldsymbol{l}|$ and $l^2 \sim 1 \rightarrow \boldsymbol{l} \cdot \dot{\boldsymbol{l}} \sim 0$[30–34]. In addition, these terms coupled with anisotropy energies can be ignored because $|K_x|$ and $|K_z| \ll D_y < J$. Taking cross product of $\boldsymbol{l}$ in equation (4), we obtain the analytical relations between $\boldsymbol{m}$ and $\boldsymbol{l}$:

$$\frac{\dot{\boldsymbol{l}} \times \boldsymbol{l}}{2J/\hbar} \sim \left(\frac{-D_y l_z}{2J}, \frac{-l_z\dot{l}_x + l_x\dot{l}_z}{2J/\hbar} + \frac{g u_B h_y}{2J}, \frac{D_y l_x}{2J} \right) = \boldsymbol{m} \tag{5}$$

Because m_x (or m_z) is only coupled with l_z (or l_x), we anticipate $\boldsymbol{l}$'s dynamics through the slave vector, $\boldsymbol{m}$. The dynamic equation of motion in G-mode is described in detail in the Supplementary information.

In S-mode, $\boldsymbol{m}$ appears to precess along the y-axis in a manner similar to ferromagnet precession in Fig. 1(d). However, the precession of $\boldsymbol{m}$ is combined with fluctuating motion with two different origins. For example, m_y is caused by the precession of excited simple antiferromagnet, as in Fig. 1(c). That is, when sub-lattice spins are precessing symmetrically along anisotropic field directions, the magnetic component parallel to the magnetic field direction is in-phase and reinforced, but the other is out-of-phase and cancelled out. However, m_x and m_z are induced by asymmetric motion of spins because of DM torque. Therefore, the two-dimensional trajectory, m_{xy}, is inherently elliptical.

Substituting m_y in equation (5) into equation (3), we have the 2D pendulum equation on $\boldsymbol{l} = (l_x, l_z) = (\cos[\varphi], \sin[\varphi])$:

$$\ddot{\varphi} + \dot{\varphi} 2\alpha J/\hbar + \sin[2\varphi]\omega_{\text{Sigma}}^2/2 = \gamma \dot{h}_y, \tag{6}$$

where $\omega_{\text{Sigma}}^2 = 2J(K_x - K_z)/\hbar^2$. Equation (6) is identical to the equation of motion in simple antiferromagnets because same effective variables are used. In S-mode, the role of DM interaction is to create m_z ($\sim l_x$) and $m_x(\sim l_z)$ components, whereas in G-mode, DM interaction lifts the degeneracy of simple antiferromagnets (see the Supplementary information). Although LLG equations are the first-order differential equation of motion with respect to time, the equation of motion for antiferromagnets is of second order because $J > 0$. Therefore, we could expect inertia-like motion.

Results and Discussion

Field-interaction regime. Both models are numerically calculated with the time interval of $\Delta t = 0.01$ ps and in a time window of $15 \text{ ps} \leq t \leq 35 \text{ ps}$. A Gaussian-type magnetic pulse, $h_y(t)$, in the form of $h_y(t) = H_0 \exp\left[-\frac{(t - t_0)^2}{2\sigma_t^2}\right]$, is applied for a center of peak with $t_0 = 20$ ps and temporal pulse width, $\sigma_t = 1$ ps. We choose the parameters for peak amplitude, H_0 and α, to be $[H_0, \alpha] = [1 \text{ Oe}, 0]$ for excitation mode and $[1 \text{ T}, 0.001]$ for switching mode, respectively. Here, damping constants, $\alpha = 0, 0.001$ are arbitrarily chosen to focus on the interplay between dh/dt and magnetization although estimated damping constant for YFeO$_3$ is 0.0003. The parameters, $\boldsymbol{l}$ and $\boldsymbol{m}$ in the pendulum model (open circle), are produced from the resultant $\varphi(t)$ with a relation to equation (5) and are found to be identical to those in LLG model (solid line). The equation of motion of pendulum confirms that the differential field, $dh_y(t)/dt$, functions as driving torque where the differential form of Gaussian pulse is of single-cycle shape. As a result, m_z and m_x (or l_x and l_z) are tipped twice, as denoted by 1 and 2 (see Fig. 2(a) and (b)). These consecutive tips occur resonantly via the single-cycle torque of $dh_y(t)/dt$.

Note that m_y is coupled with l_x and l_z, together with the field-induced magnetization, $\Delta m_y = g u_B h_y/(2J)$ in equation (6). When Δm_y is removed, we can easily see the consecutive tips in m_y, as shown in Fig. 2 (open green circles). Experimentally, Δm_y would be included in a transient Faraday rotation signal (linearly proportional to $\boldsymbol{m}$) as a strong transient in the canted antiferromagnet[35AQ1–38], or simple antiferromagnet[39]. Assuming that the other optical effects associated with the strong transients are completely excluded, the exact phase or the maximum amplitude of $\boldsymbol{l}$ should be observed in Faraday rotation signal without Δm_y.

To examine the switching process, we analyse canted antiferromagnet dynamics energetically. Two static magnetic fields of $H = 6.5$ T are turned on along the y-axis at $t = 20$ ps and one of them is turned off after $\Delta t = 2$ ps. Several energy differences are defined and plotted in the fourth row of Fig. 3(a,b): exchange gain, $\Delta E_E = 2J[\boldsymbol{s}_1(t) \cdot \boldsymbol{s}_2(t) - \boldsymbol{s}_1(0) \cdot \boldsymbol{s}_2(0)]$, anisotropy barrier, $\Delta E_A = -\{K_x[s_{1,x}(t)^2 + s_{2,x}(t)^2] - K_z[s_{1,z}(t)^2 + s_{2,z}(t)^2]\}$, and Zeeman energy, $\Delta E_Z = g u_B[\boldsymbol{s}_1(t) + \boldsymbol{s}_2(t)] \cdot h_y\hat{y}$. So far, it is known that the inertia-driven switching occurs once ΔE_E, accumulated from a decrease of ΔE_Z, overcomes potential barrier[13]. For a system with two anisotropies as like YFeO$_3$, the potential barrier is estimated as $|2(K_x - K_z)/K_x| = 1.1$ (see the fourth low of Fig. 3(a,b)). Although both excitations show identical behaviour until $t = 22$ ps, the trajectory of m_z confirms that $dh/dt|_{t=22ps}$ (see Fig. 3(a)) contributes to magnetization switching. As long as the field is turned on, any torque does not occur
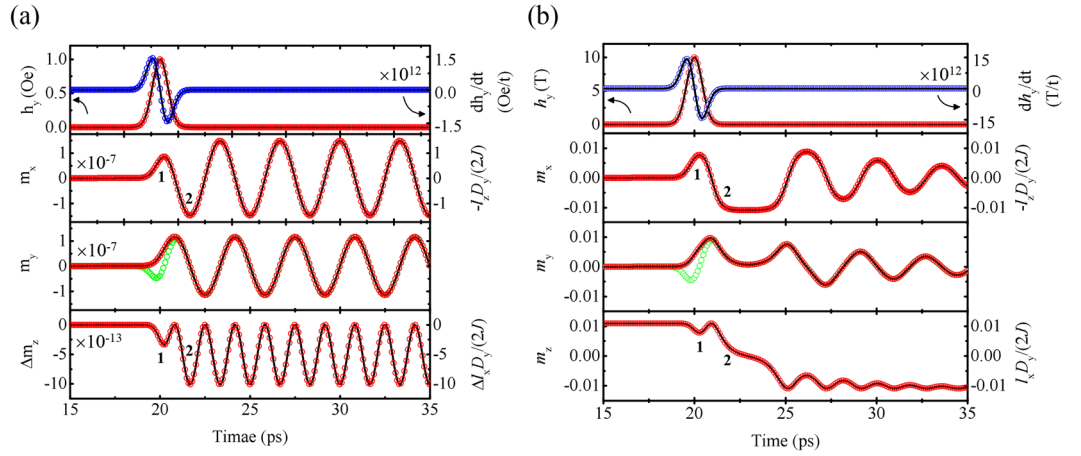
Figure 2. Analytical and numerical calculation results. (**a**) Excitation modes and (**b**) switching modes via a Gaussian-type magnetic pulse in a canted antiferromagnet. The solid line and open circles represent the numerical and analytical solution, respectively. Note that two tipping processes, denoted by 1 and 2 in m_z and m_x, are ascribed to the resonant effect by a single-cycle differential field, dh_y/dt (blue), not by h_y (red). Magnetization switching occurs by process 2. m_y also shows two tipping processes (green) when the field-induced magnetization, $\Delta m_y = gu_B h_y/(2J)$, is excluded.
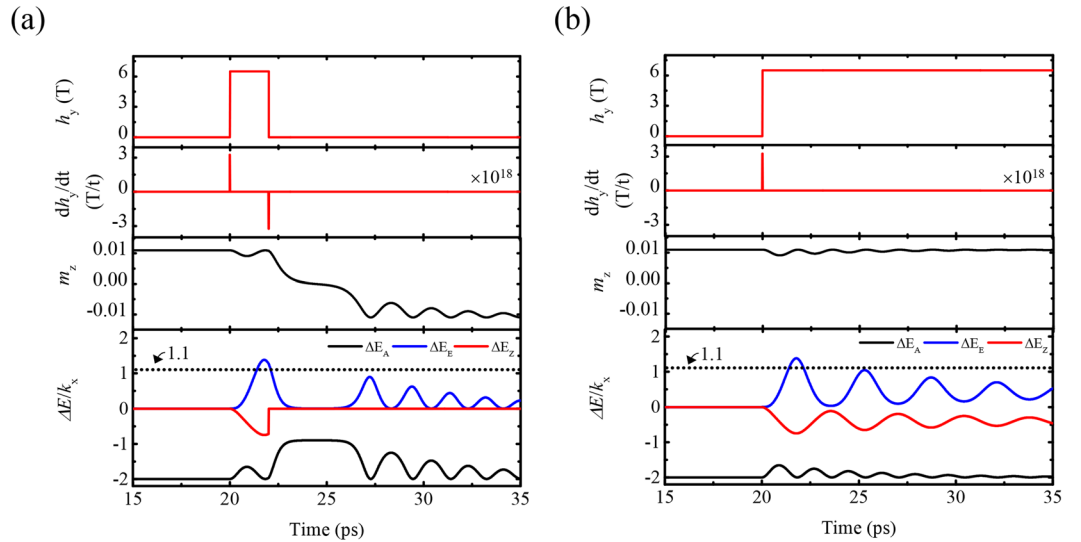
Figure 3. Energetic analysis for switching mode and non-switching mode using two different magnetic fields in canted antiferromagnets. The differential fields, dh_y/dt in two dynamic modes are of single-cycle (**a**) and half-cycle (**b**) forms. Three energy differences (exchange, anisotropy and Zeeman energies) are plotted as $\Delta E_E = 2J[s_1(t) \cdot s_2(t) - s_1(0) \cdot s_2(0)]$, $\Delta E_A = -\{K_x[s_{1,x}(t)^2 + s_{2,x}(t)^2] - K_z[s_{1,z}(t)^2 + s_{2,z}(t)^2]\}$ and $\Delta E_Z = gu_B[s_1(t) + s_2(t)] \cdot h_y \hat{y}$ respectively.

because $|dh/dt| = 0$. Therefore, the strict phase matching between l and $\gamma \dot{h}$ (or $\sim p(t)$ of Slonczewski-type spin transfer torque[16, 34]) plays a main role in the switching process.

Free induction decay regime. Next, we focus on the spin dynamics, which is driven only by an internal field ($h_y = 0$). In particular, the precessional trajectory of S-mode provides the information of DM energy as described in equation (5). With the consideration of experimental condition, where DC magnetic field of $h_{z,DC} \sim -97.5$ Oe is applied along the z-axis for magnetization saturation, equation (6) is changed as

$$m \sim \left(\frac{-D_y l_z - gu_B h_{z,DC} l_z l_x}{2J}, \frac{-l_z \dot{l}_x + l_x \dot{l}_z}{2J/\hbar}, \frac{D_y l_x + gu_B h_{z,DC} l_x^2}{2J} \right)$$
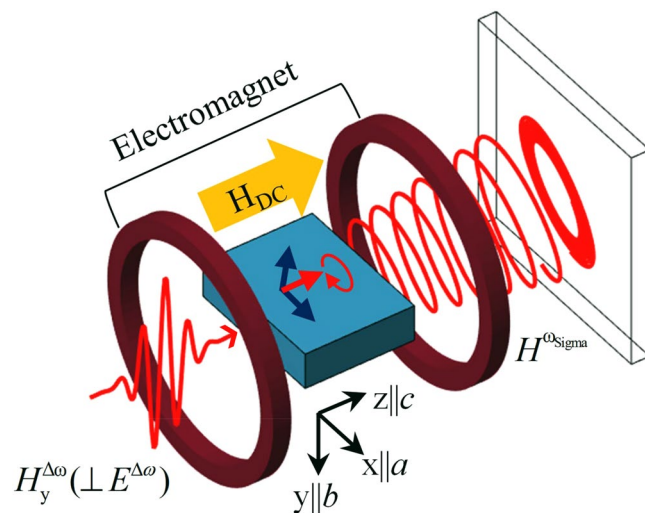
(7)

Figure 4. Schematic diagram for THz emission in YFeO$_3$ after excitation by a vertically polarized magnetic pulse of light, $H_y^{\Delta\omega}$. When $H_y^{\Delta\omega}$ is incident on the sample, the magnetizations are tilted away from their equilibrium position; subsequently, they return to the original position, precessing at a frequency of 0.3 THz via the internal magnetic field, and emitting a free-induction decay signal as the elliptically polarized light. Here, the DC magnetic field, $h_{z,DC}$, from the Helmholtz-type coils is used for magnetization saturation in the direction of the -z-axis or the crystalline c-axis. We set the crystalline axes, a, b, and c to correspond to the Cartesian axes, x, y, and z.
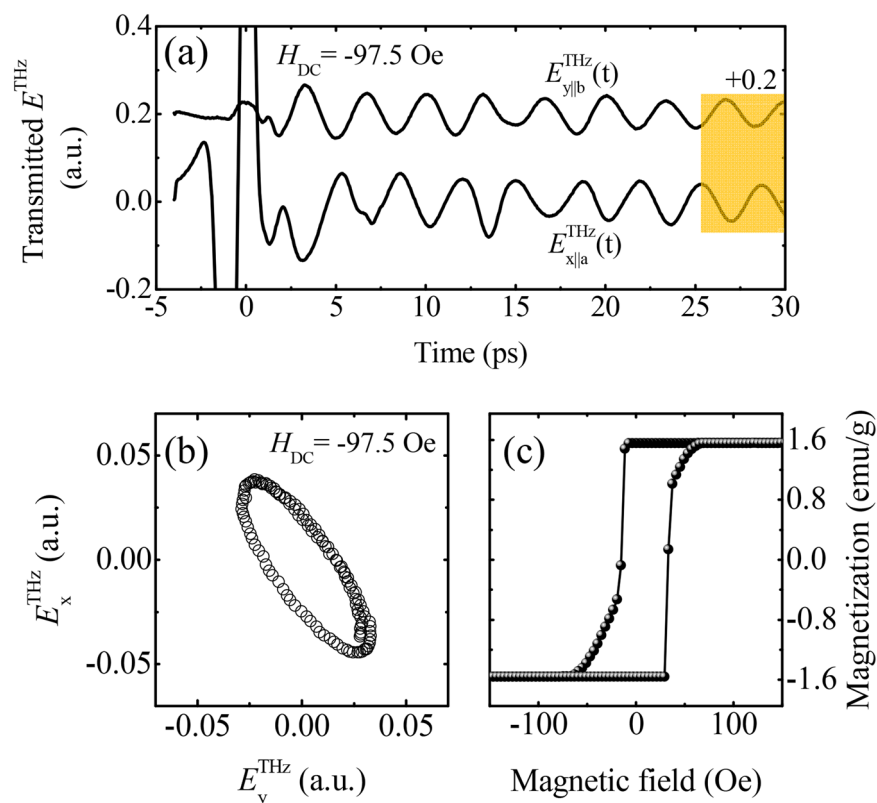

Figure 5. THz emission waves and magnetic hysteresis curve. (**a**) THz waveforms transmitted through the sample when the magnetic field is parallel to the y-axis. YFeO$_3$ is saturated fully under the external magnetic field of -97.5 Oe. $E_{x\|a}^{THz}$ and $E_{y\|b}^{THz}$ are extracted using a pair of wire-grid polarizers set at 45° and $-45°$ from the x-direction. Here, $E_{y\|b}^{THz}$ is shifted upward by $+0.2$ for clarity. (**b**) Two-dimensional trajectories of emissions in a temporal window between 25 ps and 30 ps. (**c**) Magnetization hysteresis curve measured using a sample vibrating magnetometer. All data are quoted from ref. 40.
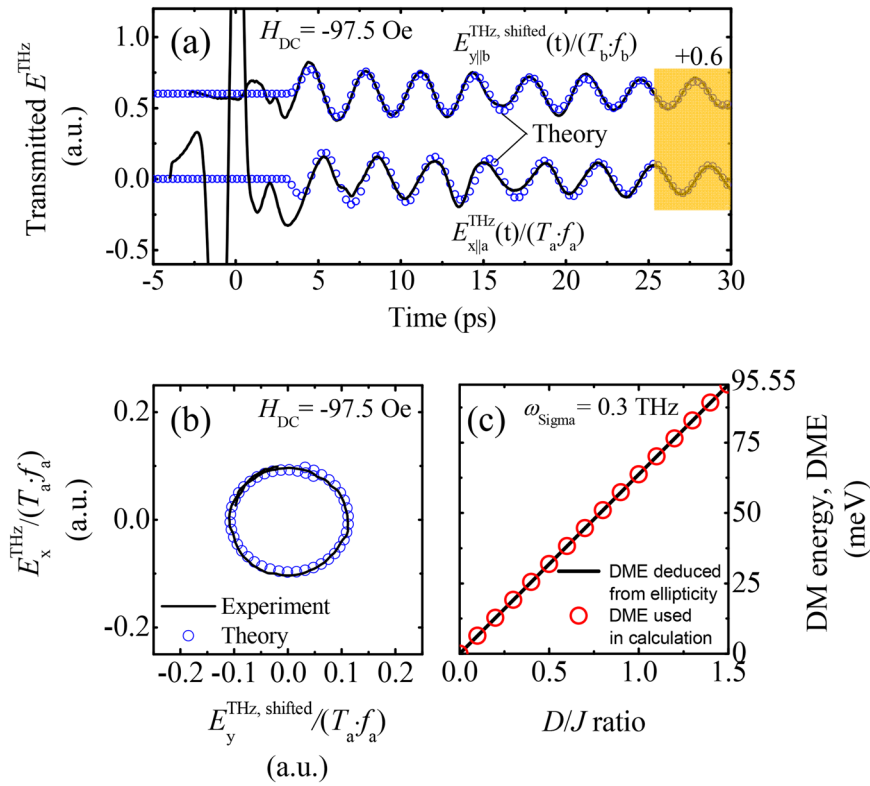
Figure 6. THz emissions scaling linearly with the spin wave trajectories and simulations. (**a**) $E_{y\|b}^{THz,shifted}$ is the temporal waveform shifted by $-1.15\,ps$ from $E_{y\|b}^{THz}$ because of the refractive index difference, $\Delta n_{ab} = -0.23$, between the a and b axes at $0.3\,THz$. In addition, the resultant $E_{x\|a}^{THz}$ and $E_{y\|b}^{THz,shifted}$ were considered by different transmissions, $T_a = 0.41$ and $T_b = 0.35$, and phase mismatching factors, $f_a = 0.99$ and $f_b = 0.84$, which results from the interference between propagating THz pulses and emissions. (**b**) Two-dimensional trajectories of emissions in the temporal window between $25\,ps$ to $30\,ps$. In (**a,b**), the experimental results (solid line) are matched closely to the numerical ones (open circles) calculated by using the parameters extracted from the sample. (**c**) The determination of the various DM energies when the S-mode is weakly excited or a Gaussian-type magnetic pulse with $[H_0, \sigma_t, \alpha] = [1\,Oe, 1\,ps, 0]$ is applied. The DM energy used in the simulation (open circle) is comparable to one deduced from the ellipticity (solid line).

However, the magnetization dynamics are driven effectively by internal field because of $D_y \gg g u_B h_{z,DC}$ and, still, $l \gg m$. In addition, equation (6) is not changed by a weak DC-magnetic field because $dh_{z,DC}/dt = 0$. Therefore, the ellipticity, $\varepsilon \equiv |m_y|/|m_x|$, of the precessional motion is deduced as $\left[-2J/(D_y l_z)\right]\left[\hbar(-l_z \dot{l}_x + l_x \dot{l}_z)/(2J)\right]$ $\sim C\hbar\omega_{Sigma} \cos[\omega_{Sigma}t]/\left(D_y \sin[C \sin[\omega_{Sigma}t]]\right)$ and, thereby, $\sim \hbar\omega_{Sigma}/(D_y \tan[\omega_{Sigma}t])$ when the S-mode is weakly excited or $\varphi \sim C \sin[\omega_{Sigma}t]$ is small.

Our analytical approaches to YFeO$_3$ are appropriate because D_y/J ratio is weak enough or canting angle, β, is small where $\beta = \arctan[m_x/l_x] = \arctan[D_y/(2J)] \sim 0.6$ degrees. As the D_y/J ratio increases, the pendulum model deviates gradually from LLG model. At room temperature, the antiferromagnetic spin state of YFeO$_3$ is illustrated in Fig. 1(a). YFeO$_3$ exhibits two resonant modes, S-mode and G-mode[24]. Terahertz (THz) time-domain spectroscopy is used to measure the DM energy in S-mode, where we set the crystalline axes, a, b, and c corresponding to Cartesian axes, x, y, and z (see Fig. 4). When vertically polarized THz magnetic pulse ($h_y//b$) transmits through YFeO$_3$ with a thickness of $1.5\,mm$[40], l experiences a driving toque and is tilted effectively by the spectral component around resonant frequency. Simultaneously, m starts to process and oscillate along the z-axis due to internal magnetic fields. The oscillating frequency is higher by two times than the precessional frequency, while the oscillating amplitude is negligible in weak excitation[19]. Precession motion will stop eventually because of damping. This is called as free-induction decay process. Actually, the precession of magnetization emits an electromagnetic or emission wave and a photoconductive antenna detects it.

In experiment, free-induction decay signals under $h_{z,DC} \sim -97.5\,Oe$ for saturation are obtained, as shown in Fig. 5(a), where the raw data are quoted from ref. 40. Here, the incident THz electric field is linearly polarized along the x-axis, and detector is only sensitive to the x-component of electric field of emission wave. Therefore, a wire grid polarizer is used to extract the y-component. After THz field passed through polarizers with the angles of $+45$ and -45 degree from the x-axis, subtraction and summation of the two transmitted THz waves yield the y- and x-component of emission wave (E_x^{THz} and E_y^{THz}) in Fig. 5(a), respectively[40, 41]. However, the resultant waves are more strongly elliptical than expected (see Fig. 5(b)). They are modulated by four effects, accumulated during

propagation of emission waves through YFeO₃ crystal. First, the modulation happens due to the refractive index difference, $\Delta n_{ab} \sim -0.23$, between the a-axis and b-axis[40, 42], which results in a phase delay of $\Delta n_{ab}/c \times t \sim 1.15\,ps$ between emission waves. Second, the different absorption coefficients or transmissions, T, degrade the emission waves by the factors of $T_a \sim 0.41$ and $T_b \sim 0.35$[42]. Third, refractive index mismatch between incident THz pulse and spin wave, depending on the crystal axis, induces interference after transmission. Therefore, the factors are calculated using the cardinal sine or sinc function: $f_a \sim \mathrm{sinc}(2\pi \times 0.3\,\mathrm{THz}/c \times 1.5\,\mathrm{mm}) \sim 0.99$ and $f_b \sim \mathrm{sinc}(2\pi \times 0.3 \times 10^{12}\,s^{-1}/c \times (-0.21) \times 1.5\,\mathrm{mm}) \sim 0.84$, where c is the speed of light. Fourth, the spin wave (or emission wave) perpendicular to the incident magnetic field is significantly dependent on the magnetization state[40]. To remove this effect, we saturated magnetization by applying $h_{z,DC}$.

Figure 6(a) shows emission waves, scaled linearly with the real spin wave: $E_{x\parallel a}^{emission}/T_a/f_a$ and $E_{y\parallel b}^{emission,shifted}/T_b/f_b$. From the ellipticity of precessional trajectories in Fig. 6(b), the DM energy is estimated as $0.3 \times 10^{12}\,s^{-1} \times 2\pi \times \hbar /\varepsilon \times (1.6 \times 10^{12}\,\mathrm{J/eV})^{-1} \sim 1.4\,\mathrm{meV}$ where $\varepsilon \equiv |m_y|/|m_x| = |E_x^{THz}|/|E_y^{THz}| = 0.9178$. Here, the damping effect is ignored because of negligible contribution to the DM energy calculation. (The damping constant is estimated as 0.0003 by fitting the precessional data to LLG model and it is due to the magnon scattering on phonons and spins of Yittrium ions[9]).

The exchange energy, J, is deduced using the asymmetric exchange model[40]: $J = M_0 D_y/M_s = 72.5\,\mathrm{emu/g} \times 1.4\,\mathrm{meV}/1.54\,\mathrm{emu/g} = 63.7\,\mathrm{meV}$, where M_0 is magnetic moment of ions per unit mass, and M_s is the saturation magnetization in Fig. 5(c). The two anisotropy energies are deduced through the two resonant frequency formulas, where $\omega_{Sigma} = 0.3\,\mathrm{THz}$[15, 40] and $\omega_{Gamma} = 0.52\,\mathrm{THz}$ and found to be $K_x = (\omega_{Gamma}^2 \hbar^2 - D_y^2)/(2J) \sim 22\,\mu\mathrm{eV}$ and $K_z = K_x - \omega_{Sigma}^2 \hbar^2/(2J) \sim 9.9\,\mu\mathrm{eV}$. All parameters are in good agreement with reference[43]. Moreover, our numerical calculation using the above parameters explains the experimental data well.

Figure 6(c) shows DM energy, deducted from ellipticity in Fig. 6(b), in terms of D/J ratio, together with DM energy in calculation. When S-mode is weakly excited or a Gaussian-type magnetic pulse with $[H_0, \sigma_t, \alpha] = [1\,\mathrm{Oe}, 1\,\mathrm{ps}, 0]$ is applied, the precessional ellipticity, calculated from LLG model, determines exact DM energy. DM energy from ellipticity matches well with that in calculation up to $D_y/J = 1.5$ (or canting angle ~28 degrees), indicating that measurement of the strong DM energy through ellipticity analysis is quite effective experimental method. The value of $D_y/J = 1.5$ makes the method useful to examine the antiferromagnetic bubble and chiral domain wall dynamics and to control the DM energy through interface engineering[44]. Our experimental condition agrees with weak excitation by THz magnetic pulse. The THz electric field strength did not exceed the value of ~1 kV/cm for a focused beam size of 3 mm; therefore, the peak magnetic field was below 3 Oe. And our magnetic system is directly coupled with the magnetic field. If spin waves are excited by the electric field of THz pulse, the experimental results that Faraday rotation signals in NiO[12] and emission amplitudes in YFeO₃[15] are linearly proportional to the pump field would be conjectured to be linear magneto-electric effect. However, such coupling is not allowed in centrosymmetric system[45].

Summary

In this article, we investigate the field-driven dynamics of a canted antiferromagnet in both theory and experiment. In a field-interaction regime, the antiferromagnet dynamics are excited or switched in the strict phase matching condition between $\sim d\boldsymbol{h}/dt$ and $\boldsymbol{l}$. In a free-induction decay regime, we found that the precessional ellipticity of S-mode determines DM energy in a canted antiferromagnet system. From experimental ellipticity data, we deduced successfully the DM energy, together with static parameters (J, K_x, K_z) in YFeO₃, using terahertz time-domain spectroscopy. We expect that our results would contribute significantly to broaden our fundamental understanding on antiferromagnet dynamics.

References

1. Kaka, S. & Russek, S. E. Precessional switching of submicrometer spin valves. *Appl. Phys. Lett.* **80**, 2958 (2002).
2. Tudosa, I. *et al.* The ultimate speed of magnetic switching in granular recording media. *Nature* **428**, 831 (2004).
3. Gerrits, T., van den Berg, H. A. M., Hohlfeld, J., Bar, L. & Rasing, T. Ultrafast precessional magnetization reversal by picosecond magnetic field pulse shaping. *Nature* **418**, 509 (2002).
4. Bauer, M., Fassbender, J., Hillebrands, B. & Stamps, R. L. Switching behaviour of a Stoner particle beyond the relaxation time limit. *Phys. Rev. B* **61**, 3410 (2000).
5. Serrano-Guisan, S. *et al.* Biased Quasiballistic Spin Torque Magnetization Reversal. *Phys. Rev. Lett.* **101**, 087201 (2008).
6. Kittel, C. Theory of Antiferromagnetic Resonance. *Phys. Rev.* **82**, 565 (1951).
7. Wadley, P. *et al.* Electrical switching of an antiferromagnet. *Science* **351**, 587 (2016).
8. Kimel, A. V., Kirilyuk, A., Tsvetkov, A., Pisarev, R. V. & Rasing, T. Laser-induced ultrafast spin reorientation in the antiferromagnet TmFeO3. *Nature* **429**, 850 (2004).
9. Kimel, A. V. *et al.* Ultrafast non-thermal control of magnetization by instantaneous photomagnetic pulses. *Nature* **435**, 655 (2005).
10. Kimel, A. V. *et al.* Inertia-driven spin switching in antiferromagnets. *Nat. Phys.* **5**, 727 (2009).
11. Gomonay, H. V. & Loktev, V. M. Spin transfer and current-induced switching in antiferromagnets. *Phys. Rev. B* **81**, 144427 (2010).
12. Kampfrath, T. *et al.* Coherent terahertz control of antiferromagnetic spin waves. *Nat. Photon.* **5**, 31 (2011).
13. Wienholdt, S., Hinzke, D. & Nowak, U. THz Switching of Antiferromagnets and Ferrimagnets. *Phy. Rev. Lett.* **108**, 247207 (2012).
14. Alexej, P., Alexander, S., Tobias, K. & Rupert, H. Electric and magnetic terahertz nonlinearities resolved on the sub-cycle scale. *New J. Phy.* **15**, 065003 (2013).
15. Kim, T. H. *et al.* Coherently controlled spin precession in canted antiferromagnetic YFeO 3 using terahertz magnetic field. *Appl. Phys. Expr.* **7**, 093007 (2014).
16. Cheng, R., Daniels, M. W., Zhu, J.-G. & Xiao, D. Ultrafast switching of antiferromagnets via spin-transfer torque. *Phys. Rev. B* **91**, 064423 (2015).
17. Mikhaylovskiy, R. V. *et al.* Ultrafast optical modification of exchange interactions in iron oxides. *Nat. Commun.* **6**, 8190 (2015).
18. Tao, K., Polyakov, O. P. & Stepanyuk, V. S. Switching of antiferromagnetic chains with magnetic pulses. *Phys. Rev. B* **93**, 161412 (2016).
19. Kim, T. H., Grünberg, P., Han, S. H. & Cho, B. Ultrafast spin dynamics and switching via spin transfer torque in antiferromagnets with weak ferromagnetism. *Sci. Rep.* **6**, 35077 (2016).

20. Cheng, R., Daniels, M. W., Zhu, J.-G. & Xiao, D. Antiferromagnetic Spin Wave Field-Effect Transistor. *Sci, Rep.* **6**, 24223 (2016).
21. Kittel, C. On the Theory of Ferromagnetic Resonance Absorption. *Phys. Rev.* **73**, 155 (1948).
22. Bhattacharjee, S. *et al.* Theoretical Analysis of Inertia-like Switching in Magnets: Applications to a Synthetic Antiferromagnet. *Phys. Rev. X* **2**, 011013 (2012).
23. Dzyaloshinsky, I. A thermodynamic theory of "weak" ferromagnetism of antiferromagnetics. *J. Phys. Chem. Solids* **4**, 241 (1958).
24. White, R. M., Nemanich, R. J. & Herring, C. Light scattering from magnetic excitations in orthoferrites. *Phys. Rev. B* **25**, 1822 (1982).
25. Tokura, Y. & Kida, N. Dynamical magnetoelectric effects in multiferroic oxides. *Phil. Trans. R. Soc. A* **369**, 3679 (2011).
26. Mochizuki, M. & Nagaosa, N. Theoretically Predicted Picosecond Optical Switching of Spin Chirality in Multiferroics. *Phys. Rev. Lett.* **105**, 147202 (2010).
27. Tokunaga, M. *et al.* Magnetic control of transverse electric polarization in $BiFeO_3$. *Nat. Commun.* **6**, 5878 (2015).
28. Hothersall, D. C., Jones, G. A. & Grundy, P. J. The detection of bubble domains in $YFeO_3$ by scanning electron microscopy. *J. Phys. D* **5**, 440 (1972).
29. Shigeru, S., Toshitaka, F. & Susumu, U. Anisotropie Bubble Domain Mobility in Orthoferrite. *Jpn. J. Appl. Phys.* **14**, 1911 (1975).
30. Gomonay, E. V. & Loktev, V. M. Spintronics of antiferromagnetic systems (review article). *Low Temp. Phys.* **40**, 17–35 (2014).
31. Ivanov, B. A. Spin dynamics of antiferromagnets under action of femtosecond laser pulses (review article). *Low Temp. Phys.* **40**, 91–105 (2014).
32. Baltz, V. *et al.* Antiferromagnetism: the next flagship magnetic order for spintronics? arXiv:1606.04284 [cond-mat] (2016).
33. Cheng, R. & Xial, D. Terahertz Antiferromagnetic Spin Hall Nano-Oscillator. *Phys. Rev. Lett.* **116**, 207603 (2016).
34. Khymyn, R., Lisenkov, I., Tiberkevich, V., Ivanov, B. A. & Slavin, A. Antiferromagnetic THz-frequency Josephson-like Oscillator Driven by Spin Current. *Sci. Rep.* **7**, 43705 (2017).
35. Gonomonay, O., Jungwirth, T. & Sinova, J. High Antiferrmagnetic Domain Wall Velocity Induced by Neel Spin Orbit Torques. *Phys. Rev. Lett.* **117**, 017202 (2016).
36. Shiino, T. *et al.* Antiferromagnetic Domain Wall Motion Driven by Spin-Orbit Torques. *Phys. Rev. Lett.* **117**, 087203 (2016).
37. Reid, A. H. M., Rasing, T., Pisarev, R. V., Dürr, H. A. & Hoffmann, M. C. Terahertz-driven magnetism dynamics in the orthoferrite $DyFeO_3$. *Appl. Phys. Lett.* **106**, 082403 (2015).
38. Mukai, Y., Hirori, H., Yamamoto, T., Kageyama, H. & Tanaka, K. Nonlinear magnetization dynamics of antiferromagnetic spin resonance induced by intense terahertz magnetic field. *New. J. Phys.* **18**, 013045 (2016).
39. Baierl, S. *et al.* Terahertz-Driven Nonlinear Spin Response of Antiferromagnetic Nickel Oxide. *Phys. Rev. Lett.* **117**, 197201 (2016).
40. Kim, T. H. *et al.* Magnetization states of canted antiferromagnetic $YFeO_3$ investigated by terahertz time-domain spectroscopy. *J. Appl. Phys.* **118**, 233101 (2015).
41. Nakajima, M., Namai, A., Ohkoshi, S. & Suemoto, T. Ultrafast time domain demonstration of bulk magnetization precession at zero magnetic field ferromagnetic resonance induced by terahertz magnetic field. *Opt. Express* **18**, 18260 (2010).
42. Gorodetsky, G. & Treves, D. Second-Order Susceptibility Terms in Orthoferrites at Room Temperature. *Phys. Rev.* **135**, A97 (1964).
43. Balbashov, A. M. *et al.* Soft mode and energy gap in spin-wave spectrum in a second-order orientational phase transition. AFMR in $YFeO_3$. *Sov. Phys. JETP* **66**, 174 (1987).
44. Chen, G. *et al.* Tailoring the chirality of magnetic domain walls by interface engineering. *Nat. Commun.* **4**, 2671 (2013).
45. Eerenstein, W., Mathur, N. D. & Scott, J. F. Multiferroic and magnetoelectric materials. *Nature.* **442**, 759–765 (2006).

Acknowledgements

Author Contributions

B.K.C. and T.H.K. conceived the project idea and planned the theoretical calculations and experiments. T.H.K. performed the theoretical calculations including experimental interpretation. T.H.K., P.G., S.H.H., and B.K.C. analysed the data. B.K.C. led the work and wrote the manuscript with T.H.K. The results of the theoretical and experimental findings were discussed by all co-authors.

Additional Information

Supplementary information accompanies this paper at doi:10.1038/s41598-017-04883-3

Competing Interests: The authors declare that they have no competing interests.

Publisher's note: Springer Nature remains neutral with regard to jurisdictional claims in published maps and institutional affiliations.